



ORIGINAL RESEARCH ARTICLE

# Development of EN AW-6082 Metal Foams and Stochastic Foam Modeling for the Individualization of Extruded Profiles

Florian Patrick Schäfke , Frederic Timmann, Christian Klose, André Hürkamp, Klaus Dröder, and Hans Jürgen Maier

Submitted: 14 July 2023 / Revised: 10 November 2023 / Accepted: 22 November 2023 / Published online: 20 December 2023

Lightweight design and hybrid components enable innovative and new component concepts, especially when combining structurally reliable metal components with individualized polymer components. In this research, a process for additive manufacturing polymers on the surface of extruded aluminum profiles is examined. The extrusion process is adapted to produce foamable aluminum profiles, which can be utilized to enable a form fit between the two materials and ensures sufficient bond strength. For this purpose, a novel aluminum block material based on the standard wrought alloy EN AW-6082 was developed. It consists of a solid EN AW-6082 core and powder metallurgically produced outer layer, which allows local foaming of the aluminum profile surface. The main objective of this study was to optimize the bond strength of the hybrid aluminum-polymer components. The methods employed include fabricating aluminum test specimens, performing mechanical tests, x-ray microscopy to analyze the pore structure and evaluating the 3D pore distribution and the wall thickness. Virtual foam models were created to numerically investigate suitable pore sizes and foam geometries for form-fit with the polymer. The porosity achieved as a function of the processing of the components are discussed and a comparison is made between the real and virtual pore structures.

**Keywords** additive manufacturing, aluminum foam, compression test, virtual foam model, x-ray microscopy

## 1. Introduction

Lightweight design offers promising solutions for resource-efficient and sustainable development and production of technical functional structures. A promising lightweight design strategy lies in the combination of different materials to create integrated hybrid structures made of metal and thermoplastic polymers. The tailored combination of specific material properties can result in weight-optimized and individualized hybrid structural components and functional structures (Ref 1-3). In the context of manufacturing individualized hybrid functional structures in large quantities, a possible solution is to combine continuous and additive manufacturing. Furthermore, the bonding of dissimilar materials in the manufacturing process often represents a central challenge. The new approach presented involves local, near-surface foaming of extruded aluminum profiles to create undercuts suitable for the mechanical interlocking of additively applied polymer materials. The

schematic process and the resulting hybrid compound are depicted in Fig. 1. Experimental and numerical investigations were performed to investigate the boundary layer and optimize the aluminum foam structure regarding the resulting bond strength. In this context, the size of the pores in the aluminum foam is a decisive parameter. Smaller pores result in small aperture radii, which significantly impair the flow of the polymer melt into the pores. For a positive contribution to the bond strength of the boundary layer, a pore should be completely filled with the polymer and exposed at the upper half. In this context, investigations on metal foam production from a wrought aluminum alloy of EN AW-6082 were carried out. The aluminum alloy EN AW-6082, which is used in the extrusion sector for the production of profiles due to its good formability and good mechanical properties, has not yet been used for metal foams. Occasional foaming tests have been carried out with AA 6061, which is similar in chemical composition to EN AW-6082 (Ref 4). Typically, pure aluminum or cast alloys such as AlSi12, AlSi10 or the patented alloy AlMg4(± 1)Si8(± 1) (Ref 5) are used for the production of aluminum foams (Ref 6-8). The manufactured test specimens in the present study were analyzed using x-ray microscopy (XRM) and the mechanical strengths were determined in compression tests. In order to use the information from the foaming study within a material-efficient, simulation-based process design, the characterization of the foam structure in the test specimen was used to create a virtual aluminum foam model. The virtual foam model was validated with respect to the median of the pore size distribution and the mean wall thickness. In the literature, there exist already several approaches to model the geometry of foam structures. Kelvin cells with varying wall thickness and Weaire-Phelan structures

Florian Patrick Schäfke, Christian Klose, and Hans Jürgen Maier, Institut für Werkstoffkunde (Materials Science), Leibniz University Hannover, An der Universität 2, 30823 Garbsen, Germany; and Frederic Timmann, André Hürkamp, and Klaus Dröder, Institute of Machine Tools and Production Technology, Technische Universität Braunschweig, Langer Kamp 19b, 38106 Braunschweig, Germany. Contact e-mail: schaefer@iw.uni-hannover.de.

## Schematic process

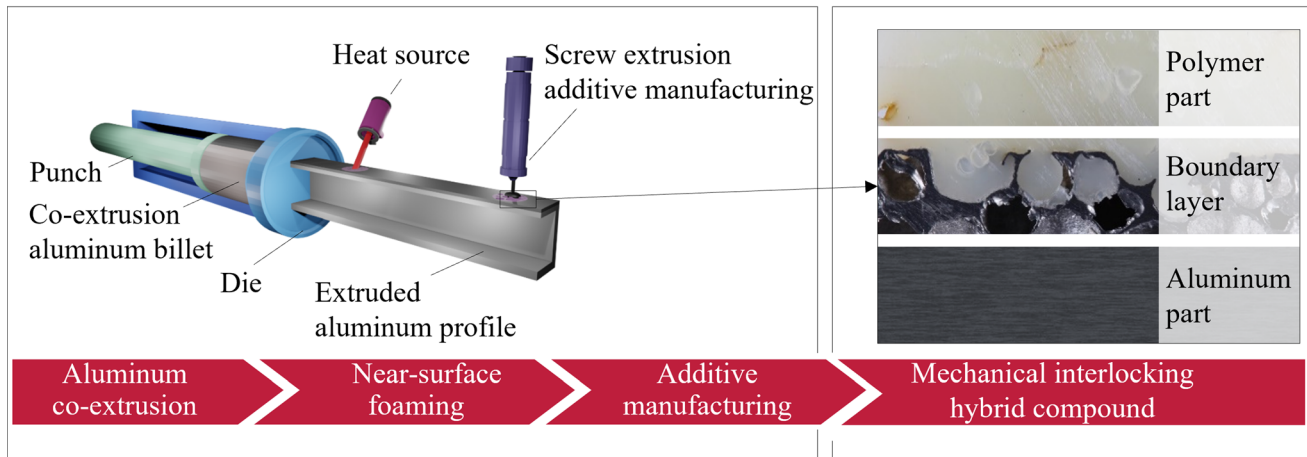


**Fig. 1** Schematic process combining continuous and additive manufacturing

which tilt space by equal volume cells are commonly used approaches (Ref 9-11). In addition, the hollow pentagonal dodecahedron model and the simple truss model can be used to model open cell foam structures (Ref 12, 13). Within the present study, a geometric model of a closed-cell aluminum foam with varying pore sizes was needed. For this purpose, a model approach based on the Voronoi diagram has shown the best results (Ref 14-16). These models are often validated with the porosity of the test specimens. In the present context, the global porosity provides not enough information about the pore structure in the boundary layer. This led to a novel approach for model validation using a geometrical analysis based on XRM to determine the pore size distribution and the mean wall thickness.

## 2. Methods and Materials

### 2.1 Experimental

In the present study, EN AW-6082 powder was used to produce metal foams via a powder metallurgical production route. The powder was produced by Eckert TLS GmbH (Bitterfeld-Wolfen, Germany) using electrode inert gas atomization. The chemical composition according to the manufacturer and the nominal contents of the individual alloying elements according to DIN EN 573-3 are shown in Table 1. In addition, measurement of the fractionated powder with a particle diameter of 63-90  $\mu\text{m}$  were conducted using a “Spectromaxx LMX06” (Spectro Analytical Instruments

GmbH, Kleve, Germany) spectrometer. These results are also listed in Table 1. The powder was fractionated with a vibration sieve machine (“VS1000” from Retsch GmbH, Haan, Germany), using sieves with mesh sizes of 180, 90, 63 and 45  $\mu\text{m}$ . Sieving of the powder was performed at 50% of the maximum vibration amplitude for 30 min.

Furthermore, titanium hydride powder ( $\text{TiH}_2$ ) from Werth-Metall (Erfurt, Germany) with a specified particle size distribution of  $D_{90} = 45 \mu\text{m}$  was used as a blowing agent for the metal foam production using the powder metallurgical process route. The chemical composition according to the manufacturer is given in Table 2.

In order to analyze the influence of foam stabilizers on the porosity in foam production, silicon carbide (SiC) with a purity of 98.44 wt.% from Mineraliengrosshandel Hausen GmbH (Telfs, Austria) was added in various particle sizes and volume fractions. The sizes of the SiC particles ( $\text{O}_{\text{SiC}}$ ), which are characterized by their FEPA numbers, are provided in Table 3.

As part of this study, 16 experimental series (ES) were carried out. A experimental series consisted of 3-4 samples with the same content of blowing agent ( $\text{TiH}_2$ , wt.%) and foam stabilizer (SiC, vol.%). The blowing agent was added in untreated form and in heat-treated form. The heat treatment according to Matijasevic et al. (Ref 17-19) of 480 °C for 180 min was carried out in a resistance furnace (“N41/380” from Nabertherm GmbH, Lilienthal, Germany).

Since the temperature-time-regime for foaming was already investigated in a previous study, the experiments of the present study were designed to determine the influence of the foam stabilizer and heat treatment of the blowing agent on the foam

**Table 1** Chemical composition of the EN AW-6082 powder

Element	Si	Fe	Cu	Mn	Mg	Cr	Zn	Ti	Al
Nominal according to DIN EN 573-3, wt.%	0.7-1.3	< 0.55	< 0.100	0.4-1.0	0.6-1.2	< 0.25	< 0.200	< 0.10	Balance
Value from the manufacturer for the entire powder, wt.%	1.0	0.13	0.005	0.6	1.0	< 0.01	< 0.002	0.01	Balance
Value measured on fractionated powder (63-90 $\mu\text{m}$ ), wt.%	1.4	0.14	0.002	0.8	0.8	< 0.01	< 0.020	0.02	Balance

**Table 2 Chemical composition of the TiH<sub>2</sub> foaming agent used**

Element	Ti	Fe	H	Mg	Mn	N	O
Value from the manufacturer, wt.%	> 95.0	< 0.08	> 3.8	< 0.015	< 0.018	< 0.25	< 0.35

**Table 3 Particle diameters of the SiC powders used (manufacturer's specifications)**

FEPA-Nr.	ØSiC 3% (D3), µm	ØSiC 50% (D50), µm	ØSiC 94% (D94), µm
320	49.0	29.2	16.5
400	32.0	17.3	8.0
600	19.0	9.3	3.0

**Table 4 Parameter combinations used in the 16 experimental series**

series	TiH <sub>2</sub> , wt.%	TiH <sub>2</sub> heat treatment	SiC, vol.%	ØSiC, µm
1	0.5	None	0	...
2	0.7	None	0	...
3	0.5	480 °C for 180 min	0	...
4	0.7	480 °C for 180 min	0	...
5	0.7	480 °C for 180 min	10	29.2
6	0.7	480 °C for 180 min	10	17.3
7	0.7	480 °C for 180 min	10	9.3
8	0.5	None	5	17.3
9	0.5	None	10	17.3
10	0.5	None	15	17.3
11	0.5	480 °C for 180 min	10	17.3
12	0.7	None	10	17.3
13	0.5	None	5	29.2
14	0.5	None	7	29.2
15	0.5	None	7	17.3
16	0.5	None	7	9.3

properties (cf. Table 4). For the powder mixtures of ES 1-4, no foam stabilizer was used and the influence of the content of blowing agent and the influence of a heat treatment of the blowing agent on the foam were investigated. In ES 5-7, the influence of the particle size of the foam stabilizer was analyzed and TiH<sub>2</sub> content and SiC content were kept constant for this purpose. The influence of the content of the stabilizer was determined via ES 8-10. ES 11 and 12 were used for comparison between test series 5-7 and 8-10. ES 13-16 were based on the initial results from ES 1-12 and were carried out to validate the results and combine parameters that have a positive effect on foam quality.

The powder mixtures for the individual samples with a weight of 25 g each were compacted by uniaxial pressing to disks with a diameter of 35 mm and a height of 9.8 mm. A custom-designed vertical press setup was used, in which the recipient and the press tool were heated to 350 °C and the maximum press force of 0.8 MN was applied for 15 min. Subsequently the compacted specimens were preheated to 400 °C in an air circulation furnace ("KU120/75dTRON" from SNIJSTAAL BV, Aalsmeer, the Netherlands) and then foamed at 750 °C for 5 min in a resistance furnace ("N41/380" from Nabertherm GmbH, Lilienthal, Germany).

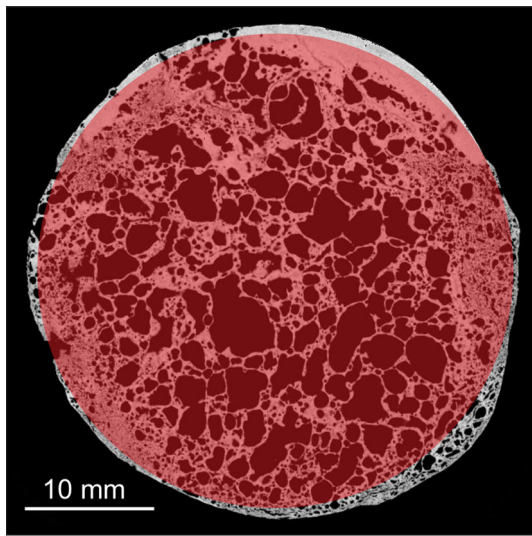
The metal foam samples obtained with this method were analyzed using an "Xradia 520 Versa" XRM (Carl Zeiss AG,

Oberkochen, Germany). A source voltage of 100 kV and a power of 10 W were used for the XRM images. Each sample was acquired in full size in a 360° scan with 3201 projections, the pixel size varied between 15 and 19 µm and the exposure time per projection between 0.8 and 1.2 s. The XRM images of the cross-sections were reconstructed into a 3D model and processed using the visualization and analysis software "Dragonfly Pro Version 2020.2". In order to determine the porosity of the metal foams from the data obtained, a region of interest (ROI) in cylindrical form was defined in the 3D model by two planar views, cf. Fig. 2. The objective was to maximize the volume of the ROI inside the 3D model resulting from the two views in the X-Y-plane and X-Z-plane. The grayscale threshold for the material segmentation was determined automatically within the software.

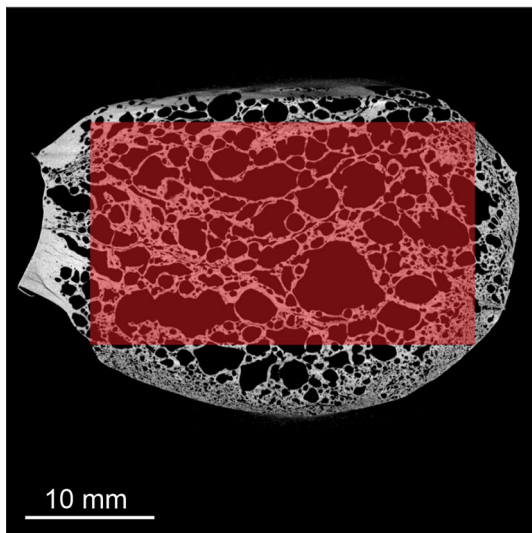
Within the specified ROI, segmentation of material and pores was performed using a threshold of gray values in the model. The porosity of the individual foam samples with the determined volumes was determined using

$$V_P = V_Z - V_M \quad (\text{Eq 1})$$

$$P = \frac{V_P}{V_Z} \quad (\text{Eq 2})$$



(a)



(b)

**Fig. 2** Representative XRM images of cross-sections of a foamed sample with the ROI marked in red; (a) X-Y section plane; (b) X-Z section plane

where  $V_P$  is the pore volume,  $V_Z$  is the cylinder volume,  $V_M$  is the material volume and  $P$  is the porosity.

The mechanical properties of the foamed samples were determined by compression tests, which were carried out in accordance with DIN 50134. Depending on the actual height of the foamed samples, the compression specimens had a height between 13 and 22 mm and were produced by wire electrical discharge machining. The diameter of the cylindrical compression specimens was then adjusted individually to obtain a length/diameter ratio of 1.5. However, the required minimum number of 10 pores in all spatial directions according to DIN 50134 was not reached by all samples due to the small dimensions of the specimens. The compression tests were conducted using a mechanical test system (“AllroundLine Z100” from ZwickRoell GmbH & Co. KG, Ulm, Germany) with a 20 kN load cell. The crosshead speed was set to  $0.01 \text{ s}^{-1}$  and the deformation was evaluated based on the crosshead

displacement. According to DIN 50134, the plateau stress ( $R_{\text{plt}}$ ) can be determined in case of a continuous stress increase as

$$R_{\text{plt}} = R_{\text{max}} - \frac{(R_{\text{max}} - R_{\text{min}})}{2} \quad (\text{Eq 3})$$

where  $R_{\text{max}}$  is the maximum stress and  $R_{\text{min}}$  is the minimum stress in the range of 20-40% compression.

## 2.2 Image Processing for Geometrical Foam Analysis of Closed-Cell Foam Structures

While the creation of grayscale images of structures via XRM is already state of the art, image processing algorithms have to be developed and used for the analysis of reconstructed geometries. In the present study, the XRM images of the aluminum foam test specimen were analyzed to determine the size and location of its pores. Cross-sectional views and porosity measurements were not sufficient for this task, as the characteristics of aluminum foam pores are a three-dimensional problem. For this purpose, the VGSTUDIO MAX software from Volume Graphics GmbH (Heidelberg, Germany) was used. With the reconstructed surface of the aluminum foam, the wall thickness and pore size distribution were determined. The foam analysis employed is based on the watershed segmentation method and separates material and void voxels within the surface mesh. The volume of each pore as well as the centroid of this volume is calculated (Ref 20).

Wall thickness is a key index for mechanical strength, and the thinnest strut region and node connectivity are the most important factors despite porosity. To calculate wall thicknesses from XRM images the ray method and the sphere method are commonly used. However, with both methods for wall thickness calculation, it is not possible to analyze the node connectivity in isolation. Therefore, the focus of the wall thickness analysis lies on the struts in the foam structure. For this purpose, the ray method was selected, which is shown schematically in Fig. 3. The algorithm searches for the closest point on the opposite surface within a search cone centered on the surface normal at each point on the object’s surface. The amount of calculated wall thicknesses is linearly related to the surface area of the detected material in the foam structure. As a result, the distribution of the wall thickness in the selected ROI is given without assignment to a specific pore or region (Ref 20).

Using the image stack from the XRM reconstructions, the methodology shown in Fig. 4 was used to determine the volumes and center location of each pore, as well as the wall thickness. Based on the gradients in the grayscale image, the surface of the material was determined. The grayscale threshold for the material segmentation is done automatically within the software. This surface was then used to calculate the wall thickness and to analyze the volume of the voids in the aluminum foam structure.

## 2.3 Model Setup of the Virtual Foam Model

The virtual foam model presented in this research is based on the Voronoi diagram. The Voronoi diagram is defined as the geometric representation of the partitioning of a plane into regions based on the distances to a set of points, shown in Fig. 5. Although it is often described in 2D, the mathematical formulation of the Voronoi diagram is valid for n-dimensions (Ref 21). The 2D and 3D Voronoi diagram have numerous applications in fields such as computer science, biology,

physics, and engineering. A survey of these applications is given by Aurenhammer (Ref 22). In Fig. 5, the generation points, the center points and the cell walls are labeled inside the Voronoi cell. A radial growth from the generation points defines the geometry of the cell wall, which separates the Voronoi cells. Due to the random distribution of generation points and the resulting irregular polyhedron, the center point of the Voronoi cell and the generation point are not congruent.

In a three-dimensional space, Voronoi cells are polyhedrons, which are used in the present study for the geometrical modeling of the defect volume in a closed-cell aluminum foam

structure. By scaling the cells, a cell wall with a defined thickness is generated. Considering the use of the Voronoi diagram to create the cells in the virtual foam model, the resulting geometry of a single Voronoi cell is a convex hull. This will lead to a virtual foam model that represents a regular closed cell aluminum foam structure. In reality, wall ruptures occur in closed-cell aluminum foam structures, which lead to more complex shapes of the cells. However, these wall rupture events are not considered in this study due to the higher modeling complexity and goal of minimizing these wall ruptures through an optimization of foaming parameters.

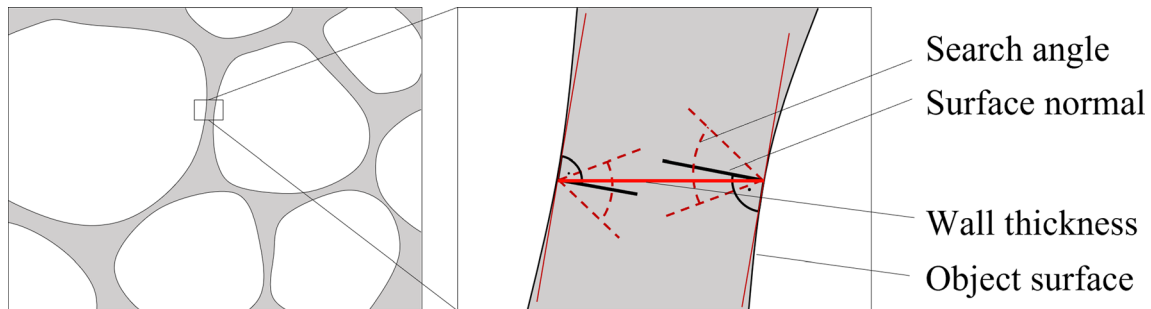


Fig. 3 Ray method for wall thickness analysis

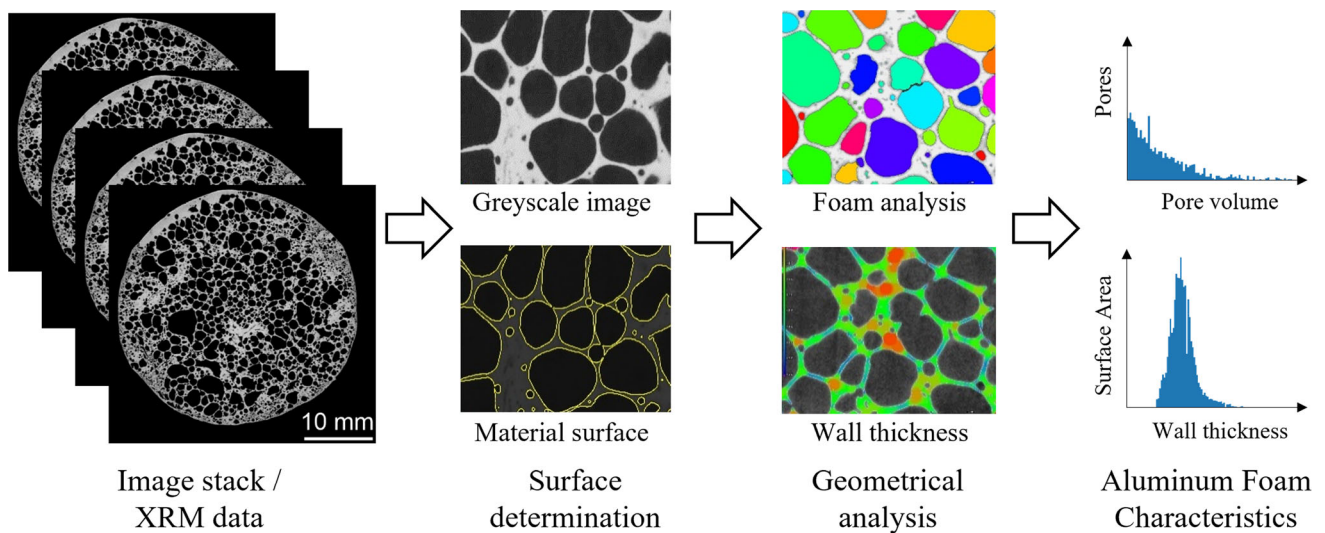


Fig. 4 Methodology for the geometry analysis of foam structures

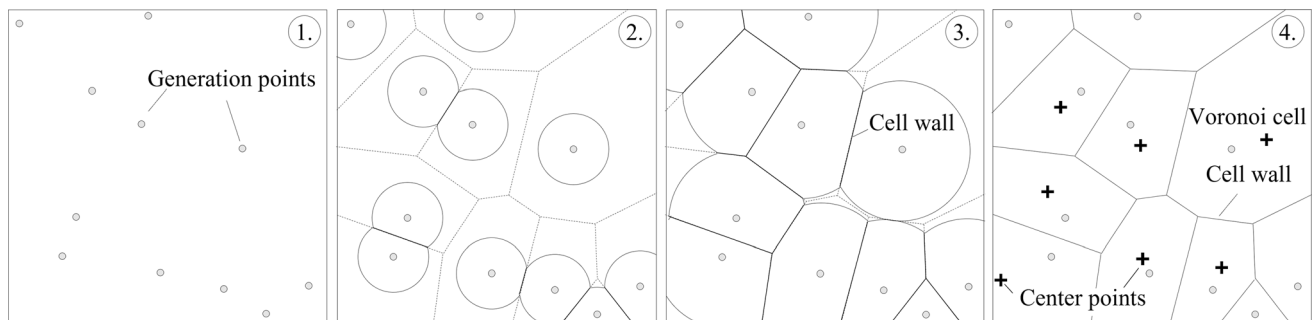


Fig. 5 Generation of a 2D Voronoi diagram

The presented virtual foam model was built in Matlab using the approach of Michailidis et al. (Ref 16). The methodology is illustrated in Fig. 6.

Starting from the randomly distributed generation point set  $\bar{P}_{gen}$ , the Voronoi diagram is constructed in a fixed volume of the Representative Volume Element (RVE)  $V_{RVE}$ . Here, the pore density can be used to influence the number of Voronoi cells, and thus their size. Since in the present study only the boundary layer of the hybrid composite was considered for the investigation, a plane was defined to select the Voronoi cells, which lies at the height of the boundary layer. This plane defines the location where the aluminum foam is exposed through a subtractive process such as milling. Furthermore, only the internal pores, without contact to the outer edges of the RVE, were considered for the geometric modeling. The total number of Voronoi cells  $n_{cells}$  are convex polyhedrons with the number of faces  $n_f$  and the number of vertices  $n_v$  describing each cell. By scaling the Voronoi cell, the wall thickness between the pores in the aluminum foam is determined. For this purpose, the scale factor  $sf_{cell}$  was introduced. Scaling was done by moving the vertices of the polyhedron along the vector

to the center  $\bar{C}$  of the cell. To achieve a designed wall thickness with a normal distributed thickness the scale factor

$$sf_{cell} = 1 - m \cdot i \quad \text{with } m \in N. \quad (\text{Eq 4})$$

is incrementally minimized for every polyhedron  $n_{cells}$ . For each increment  $m$  the scaled vertices  $\bar{v}_{cell,s}$  of one Voronoi cell are calculated with

$$\bar{v}_{cell,s} = (\bar{v}_{cell} - \bar{c}_{cell}) \cdot sf_{cell}. \quad (\text{Eq 5})$$

The wall thickness is defined by the distance

$$\frac{wt}{2} = \frac{\sum_{n=1}^{n_f} \left| (-C_{Faces}^n(-V_s) - C_{Faces}^n(-V_s)) \right|}{n_f} \quad (\text{Eq 6})$$

which is the mean of the Euclidian distances between the faces of the scaled and original polyhedron. The parameter denotes the number of faces  $n_f$  and  $\bar{C}_{Faces}^n$  is the center of the face  $n$ . The increment  $m$  is increased until the mean distance is higher or

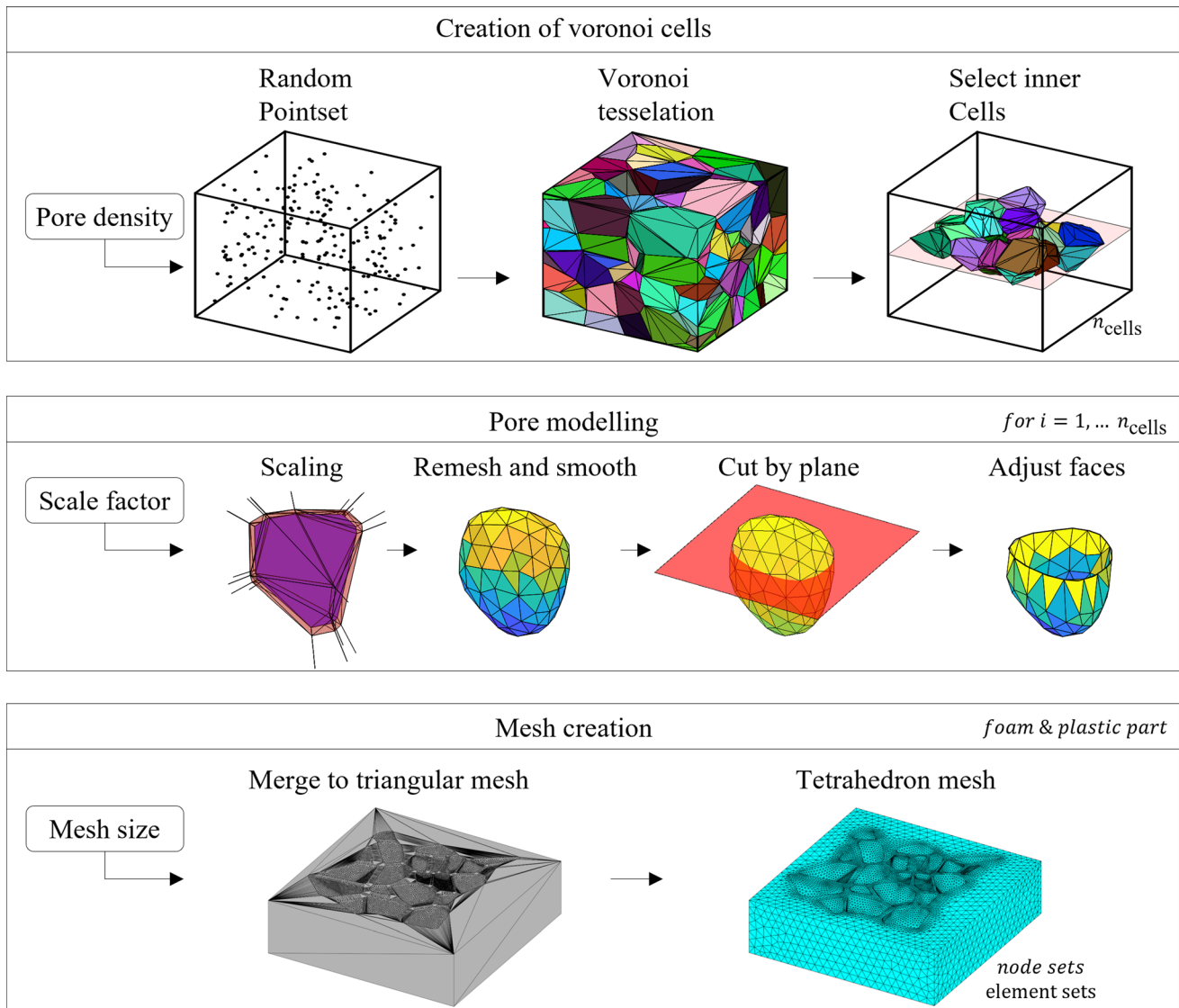


Fig. 6 Modeling approach for the virtual aluminum foam model (Ref 23)

equal to the designed wall thickness  $w_{t_{des}}$ . The faces of the scaled Voronoi cells were than subdivided into smaller uniform triangles using the subdividing scheme by Charles Loop (Ref 24). Furthermore, the polyhedron was smoothed using a Laplacian smoothing algorithm to round off the sharp corners of the polyhedron geometry (Ref 25). At the level of the defined plane, the upper half of the pore was cut off. The triangles of the mesh, which are connected with points above the cutting plane, were eliminated and the vertices at the boundary were adjusted to the level of the cutting plane. The cells were then merged to a triangular mesh with the mesh of the cuboid base part.

## 2.4 Ball Packing with Probability Density Function

The presented Voronoi-based virtual foam model requires a set of generation point set  $\bar{P}_{gen}$  to partition a volume into cells. Thus, the distribution of these points has a significant impact on the cell size of the resulting virtual foam structure. In the present study, the ball packing algorithm by Black et al. was considered (Ref 26). For the modeling of foam structures with large varying pore sizes Redenbach et al. are using a ball packing algorithm to create the generation point set (Ref 14). A probability density function is used to describe the varying sizes of the spheres, packed into the fixed volume  $V_{RVE}$ . For the volume distribution, the gamma probability function

$$f(x; \alpha, \beta) = \begin{cases} \frac{1}{\beta^\alpha \Gamma(\alpha)} x^{\alpha-1} e^{-x/\beta}, & x > 0, \\ 0, & \text{elsewhere,} \end{cases} \quad (\text{Eq 7})$$

is used, with the gamma function (Ref 27)

$$\Gamma(\alpha) = \int_0^{\infty} x^{\alpha-1} e^{-x} dx, \text{ for } \alpha > 0. \quad (\text{Eq 8})$$

Here, the parameters  $\alpha$  and  $\beta$  describes the shape of the function. The coefficients of the gamma distribution were derived from the foam analysis of the experimental series. The so-called face goal parameter,  $fg$ , describes the density of packing on the cubes outer faces, which was fixed to 0.8 for the present investigation, according to the recommendation from

Black et al. (Ref 26). The algorithm starts packing the spheres from the boundary faces to the inner part of the cube. The body goal parameter,  $bg$ , describes the density of packing inside the boundary regions of the cube. Various values of  $bg$  were investigated for the virtual models created. The ball packing method was used with the following parameters:

RVE volume:  $V_{RVE} = 20 \text{ mm} \cdot 20 \text{ mm} \cdot 20 \text{ mm}$

Face goal:  $fg = 0.80$

Body goal:  $bg = 0.50 - 0.70$

Probability density function: gamma distribution coefficients:  $\alpha, \beta$

## 3. Results

### 3.1 Compression Test Results

The average plateau stresses achieved in the compression tests for the different experimental series (ES) are shown in Fig. 7.

In Fig. 7, ES 4 shows the highest plateau stress of 91 MPa and also has the largest standard deviation with 35 MPa. The lowest plateau stress, with a value of 14 MPa, was determined for ES 5. The lowest standard deviation of 2 MPa was found in ES 6, which consisted of only one foam sample and three compression samples. The other samples in ES 6 that were produced showed cracks, so that no compression specimens could be produced from the foam. In the other experimental series, two to three foam samples were tested, each with three compression specimens. The number varied because some samples also formed a crack during foaming and were therefore excluded from further evaluation.

### 3.2 Geometrical Foam Analysis

In a first step, the samples were measured in height after foaming and a height ratio was defined for an evaluation of the height change against the initial height of 9.8 mm. The ratio height is defined as the ratio height of the foam to the height of the semi-finished product. These results are listed in Table 5.

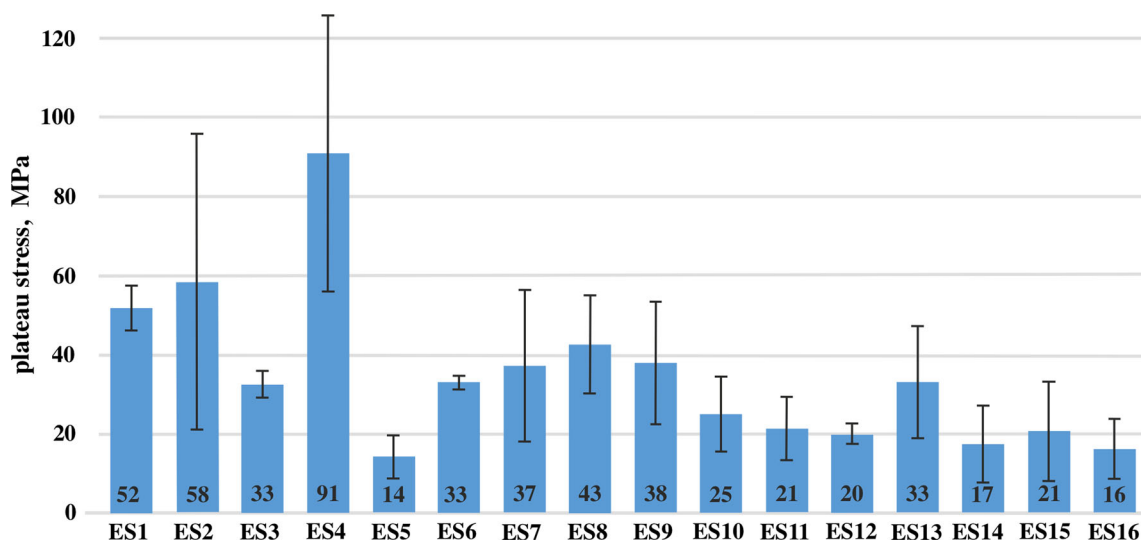
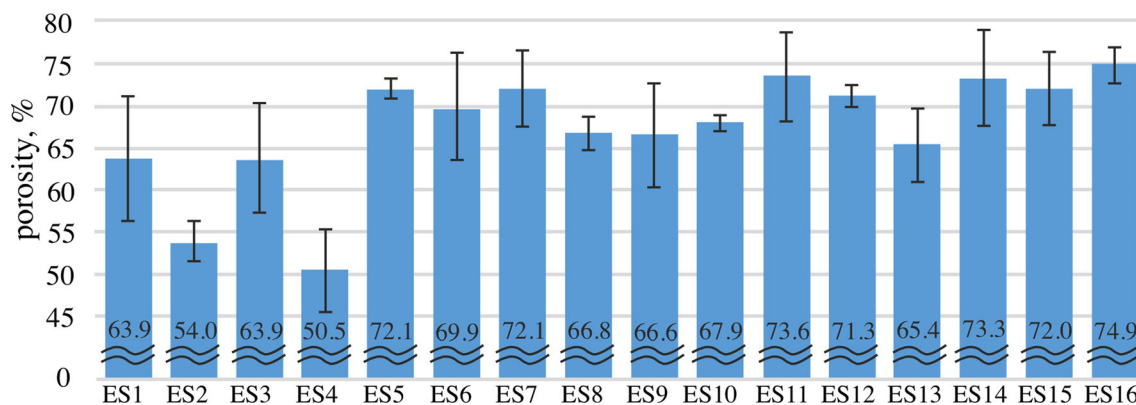


Fig. 7 Averaged plateau stresses determined for the different experimental series

**Table 5 Results of the measured sample height after foaming and the height ratio**

series	Average foam height, mm	Ratio height	series	Average foam height, mm	Ratio height
1	18.5 ± 4.0	1.9	9	24.2 ± 1.9	2.5
2	20.2 ± 3.3	2.1	10	22.5 ± 7.5	2.3
3	25.5 ± 3.4	2.6	11	26.2 ± 3.2	2.7
4	19.5 ± 1.5	2.0	12	26.4 ± 0.6	2.7
5	26.0 ± 2.3	2.7	13	24.9 ± 2.5	2.5
6	20.6 ± 3.8	2.1	14	27.0 ± 1.2	2.8
7	24.6 ± 3.0	2.5	15	27.7 ± 1.4	2.8
8	25.1 ± 1.3	2.6	16	29.8 ± 1.9	3.0

**Fig. 8** Calculated mean porosity of the individual experimental series, error bars indicate standard deviation for each series

In the further geometric analysis of the foam characteristics, ES 1, ES 8, ES 11 and ES 16 were selected based on their porosity and the foam structure evident from the cross sections.

**3.2.1 Porosity and Cross-Sections.** The Dragonfly software was used to determine the porosity of each sample based on the XRM images. Figure 8 shows the results of the porosity analysis as arithmetic mean values of the various experimental series. Based on the calculated standard deviation, the porosities within the various series differ significantly. The highest porosity was achieved for ES 16 and 11 with 74.9 and 73.6%, respectively. The lowest porosity was determined for ES 2 and 3 with 54.0 and 50.5%.

The differences in the individual porosities are due to the stochastic differences in pore formation of the individual samples during the foaming stage, which is particularly visible by the formation of globular or aspherical pores. Figure 9 and 10 show XRM cross-sections of ES 1, 8, 11 and 16. These experimental series differ in the porosity achieved and in the pore size distributions, whilst having a porosity of > 60%. Therefore, these samples appeared to be particularly well suited for the analyzes of the pore size distribution and the wall thickness analysis in Sect. 3.2 in order to validate the virtual foam model.

In Fig. 9, the samples from ES 1 show inhomogeneous and aspherical pores. The samples from ES 8 show more spherical pores than those from ES 1, although the pore size is still very inhomogeneously distributed. Across both experimental series, rather small pores occur in the peripheral areas of the samples compared to the center of the sample. The porosity, which was

determined according to Eq 2, is 60-70% in both experimental series.

In Fig. 10 most samples from ES 11 and 16 feature pores that have a rather spherical shape, whereby the distribution of pores across the sample varies even within an experimental series, so there is not a homogeneous distribution. Sample 2 of ES 11, for example, has spherical pores that are homogeneously distributed in size and position within the foam sample. Samples 1 and 3 of the same experimental series show aspherical pores as well as spherical ones and the size of the pores decreases toward the edge of the sample. All three samples of ES 16 show particular differences in pore size in the core region of the foam compared to the edge zones. Pores with an equivalent circular diameter of > 5 mm occur in the center. The decrease in pore size toward the edge zone is not constant. According to Eq 2, an overall porosity of > 70% was determined for both experimental series.

In the present study, the blowing agent content was varied between the experimental series, see Table 4. The influence of this parameter on the foam porosity is shown in Fig. 11 depending on the heat treatment of the blowing agent prior to foaming and the use of a foam stabiliser.

Figure 11 shows that a blowing agent content of 0.5 wt.% leads to a higher porosity compared to a content of 0.7 wt.%. However, the comparison between ES 9 and 12, in both of which 10 vol.% SiC were added and the blowing agent was not heat treated, shows an exception. The ES 12 with the 0.7 wt.% TiH<sub>2</sub> shows a tendency for higher porosity. Investigations by Weigand and Banhart (Ref 28) on pure aluminum and a near-

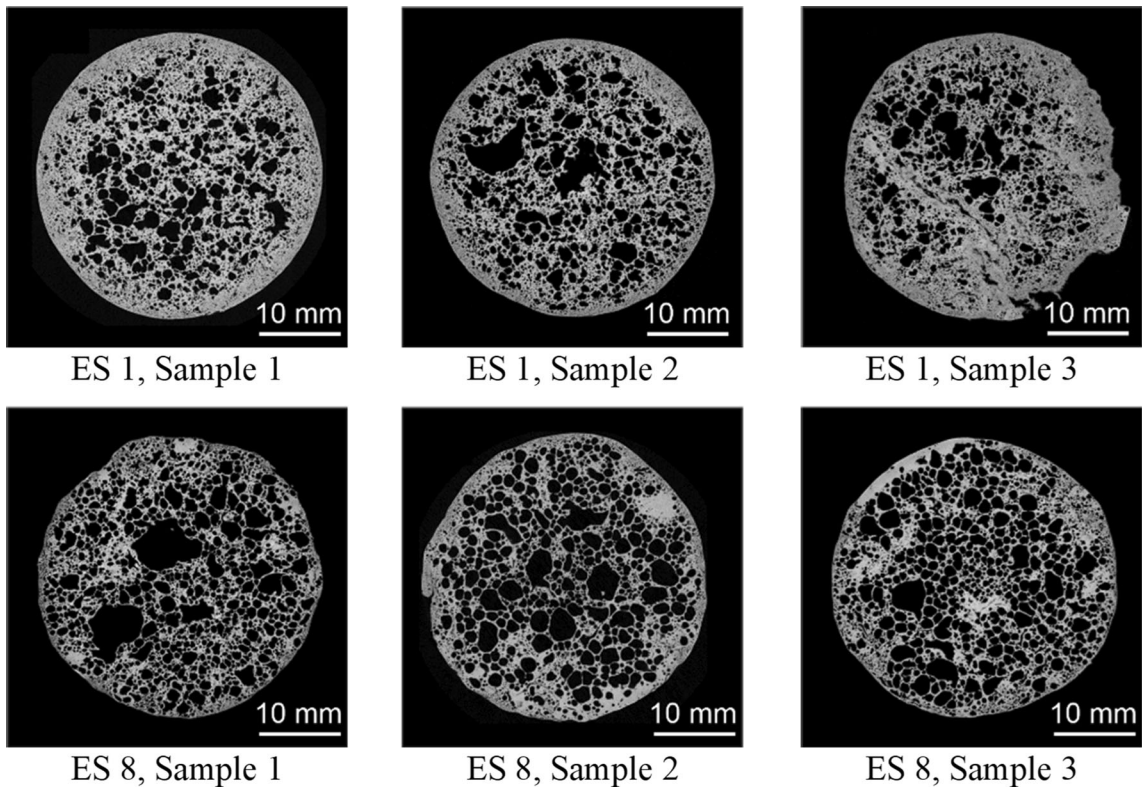


**Fig. 9** XRM cross-sectional images of sample from series 1 and 8, which are representative for series with a porosity between 60 and 70%

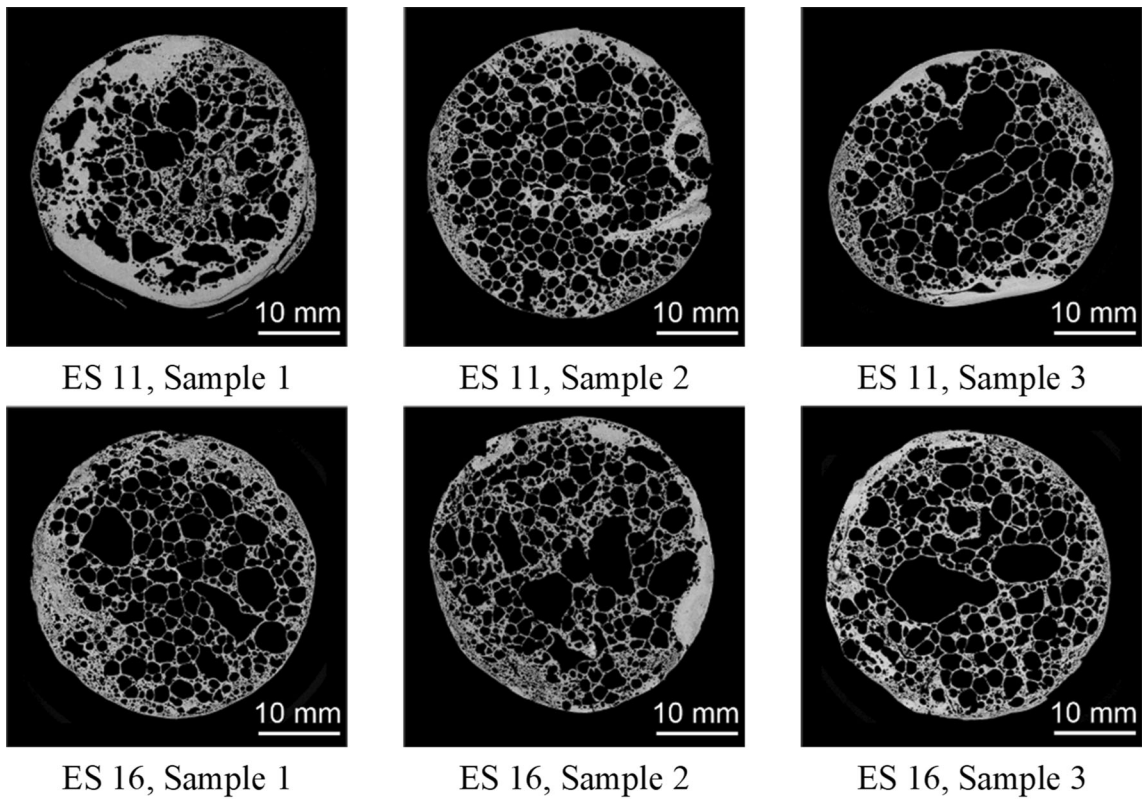


**Fig. 10** XRM sectional images of samples from experimental series 11 and 16, which are representative for test series with a porosity > 70%

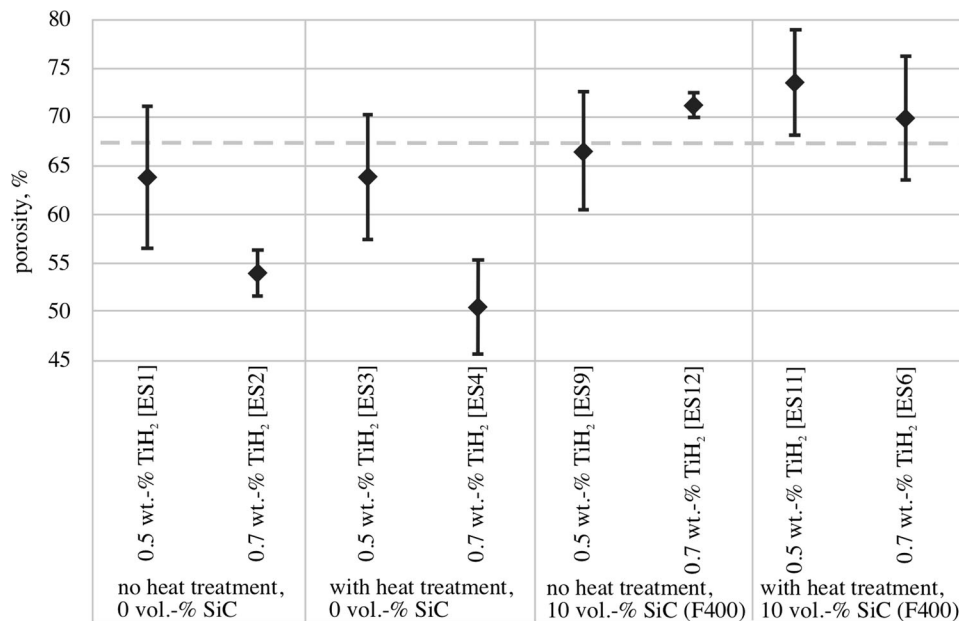


**Fig. 11** Influence of blowing agent content on the porosity of the manufactured samples; the dashed line marks the mean value of all experimental series

eutectic AlSi12 alloy showed that the maximum expansion in both alloys occurs around 0.6 wt.% TiH<sub>2</sub> and that higher blowing agent contents do not lead to greater expansion, and thus higher porosity. The larger amounts of released hydrogen are not available for a higher expansion due to diffusion processes. This behavior is also described in the literature by Lange (Ref 8) and is a possible explanation that the increased diffusion processes at 0.7 wt.% compared to 0.5 wt.% TiH<sub>2</sub> counteract a higher expansion and foam stability in the 6082-alloy used. A clear influence of the heat treatment of the blowing agent on the porosity produced is not recognizable from the data obtained. Figure 11 shows that the use of the foam stabilizer SiC leads to an increase in the achieved porosity of the foam samples made of EN AW-6082. According to the manufacturer, the average particle diameters of the SiC particles are 9.3 μm (F600), 17.3 μm (F400) and 29.2 μm (F320). An influence of the diameters on the foaming result could not be observed. According to Heim et al. (Ref 29) a stabilizing effect of SiC in the range between 0.4 and 30 μm could be achieved for AlSi9Mg0.6, which corresponds to the particle diameters used in the present study.

**3.2.2 Wall Thickness.** With the method described in Sect. 2.2, the thickness of the material between the pores was calculated. These results were used in order to match the wall thicknesses of the virtual foam models to the average wall thicknesses of the experimental series and to establish a correlation between the geometric aluminum foam structure and its mechanical strength. The wall thickness was defined in relation to the material surface for which a wall thickness could be determined within the specified search cone. Here, a cone angle of 30° was chosen. A comparison of the wall thickness distribution for two samples is shown in Fig. 12. In the cross sections on the left side of the figure, smaller and less convex pores are observed for the sample of ES 1 compared to the sample of ES 11. As a result, a tendency for more uniformly thick cell walls can be identified in the cross-section of the sample of ES 11. These differences in the geometric structure

of the aluminum foams are also observed in the diagram of the wall thickness distribution (right in the figure). To evaluate a representative value of a wall thickness for each test sample from this diagram, the wall thickness with the maximum assigned surface was chosen. According to the cross section of the sample of ES 11, the green range in the colored plot of the wall thickness is most frequently represented in the cell walls for regions with uniform foamed material. For each test sample, this maximum surface wall thickness was determined and the mean for each experimental series was used in the further investigations. The mean values of the wall thicknesses for ES 1, 8, 11, 16 are 0.17, 0.15, 0.16, and 0.13 mm, respectively.

A visualization of the evaluated cross sections and wall thicknesses is shown in Fig. 13. The wall thickness ranges from 0.08 to 0.25 mm. For all grey regions in the foam structure, no wall thickness is found within the given cone angle. In the cross-section analysis of the sample from ES 11, it can be observed that the wall thicknesses were mostly calculated for the cell walls. For the nodes characterized by larger material accumulations, less wall thicknesses are calculated by the ray method. This is in alignment with the intended goals for the application of the methodology.

**3.2.3 Cell Volume.** The foam analysis determines the cell volume distribution through a separation and categorization process for the pores in the foam structures. A cross section with the detected cells is illustrated in Fig. 14. The coloring visualizes the cell separation. All pores appear to be identifiable regardless of their size and shape. In the first sample from ES 1, a higher number of pores is observed. Larger cell sizes can be seen in the cross section of the second sample from ES 11. Wall ruptures in the aluminum foam structure lead to a poor separation of some adjacent cells. However, due to the statistical relevance, this phenomenon is not taken into account in the statistical distribution of pores.

The pore volume distributions for each of the samples are shown in Fig. 15. For an easier comparison, a logarithmic scale

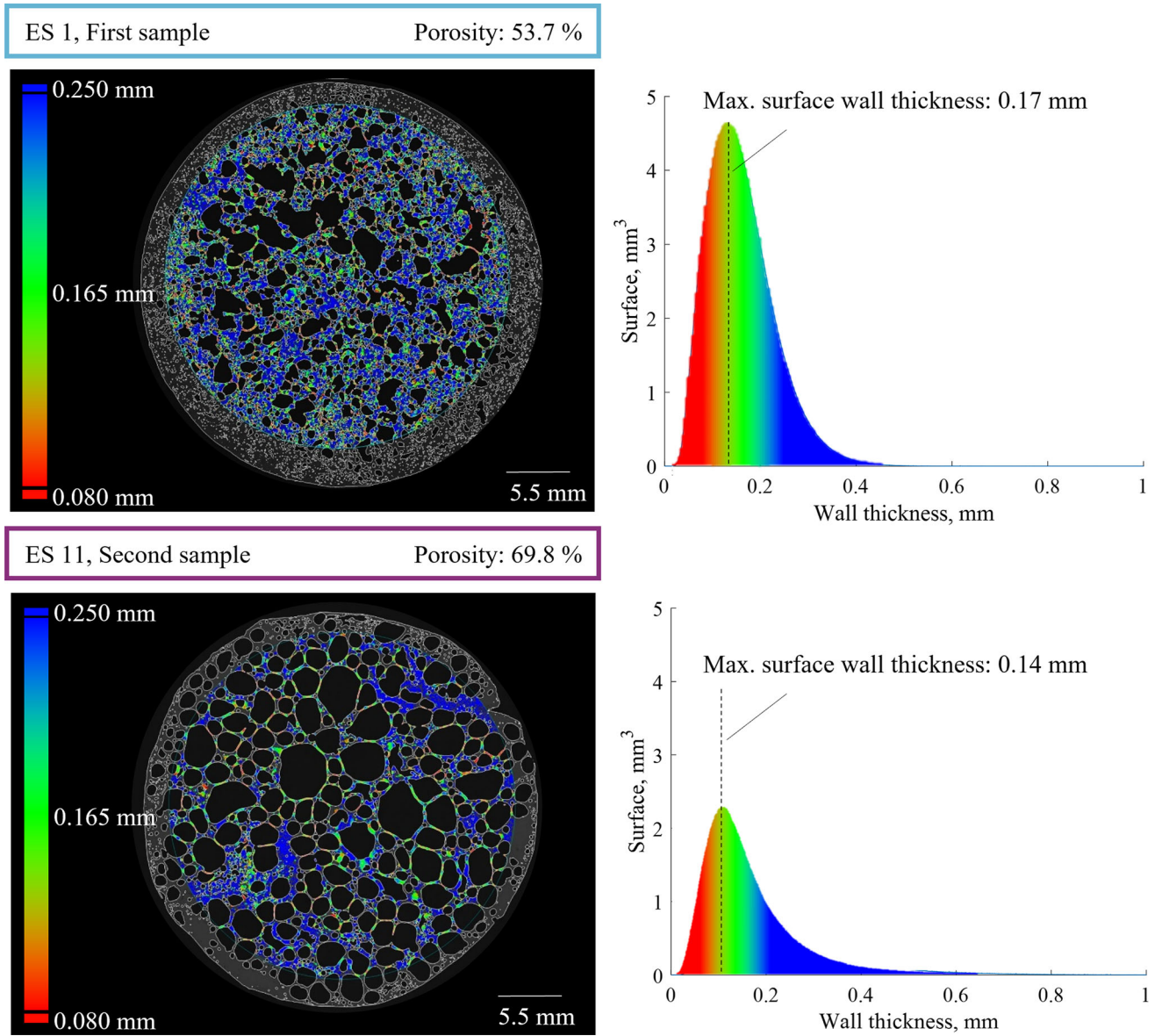


Fig. 12 Wall thickness visualization (left) and distribution of calculated wall thicknesses (right)

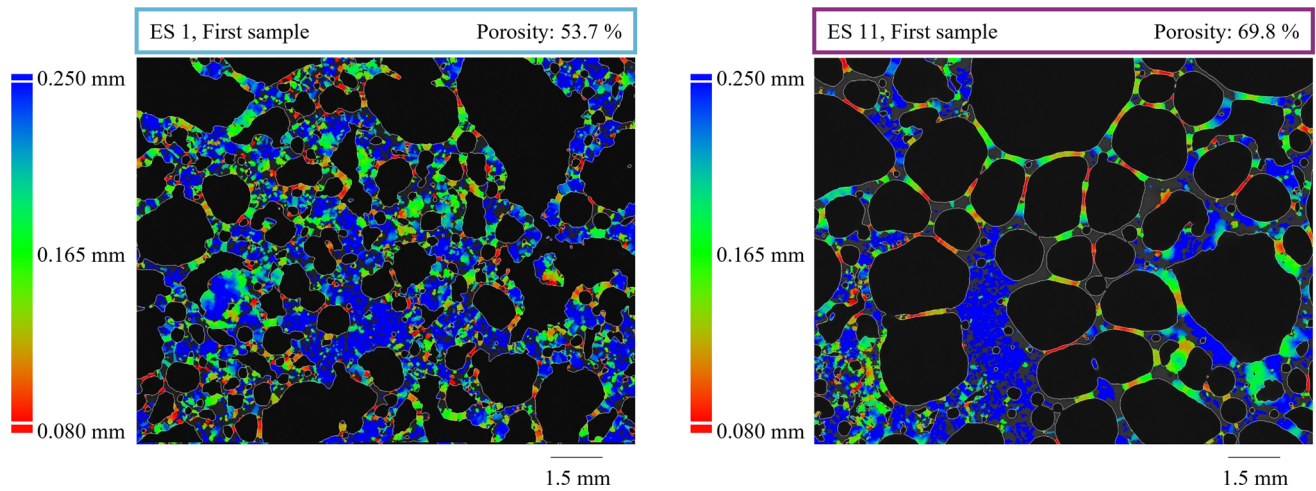
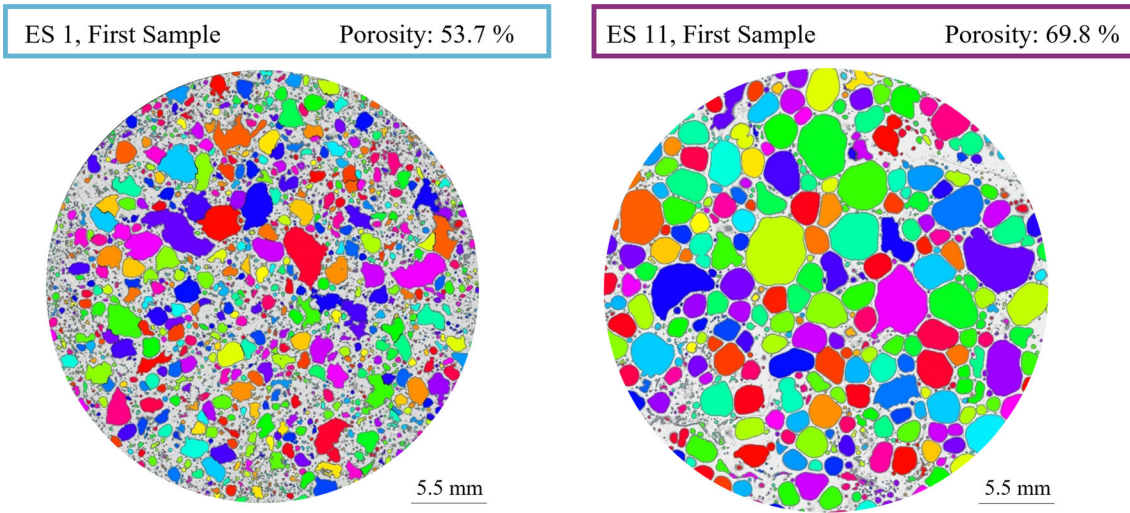
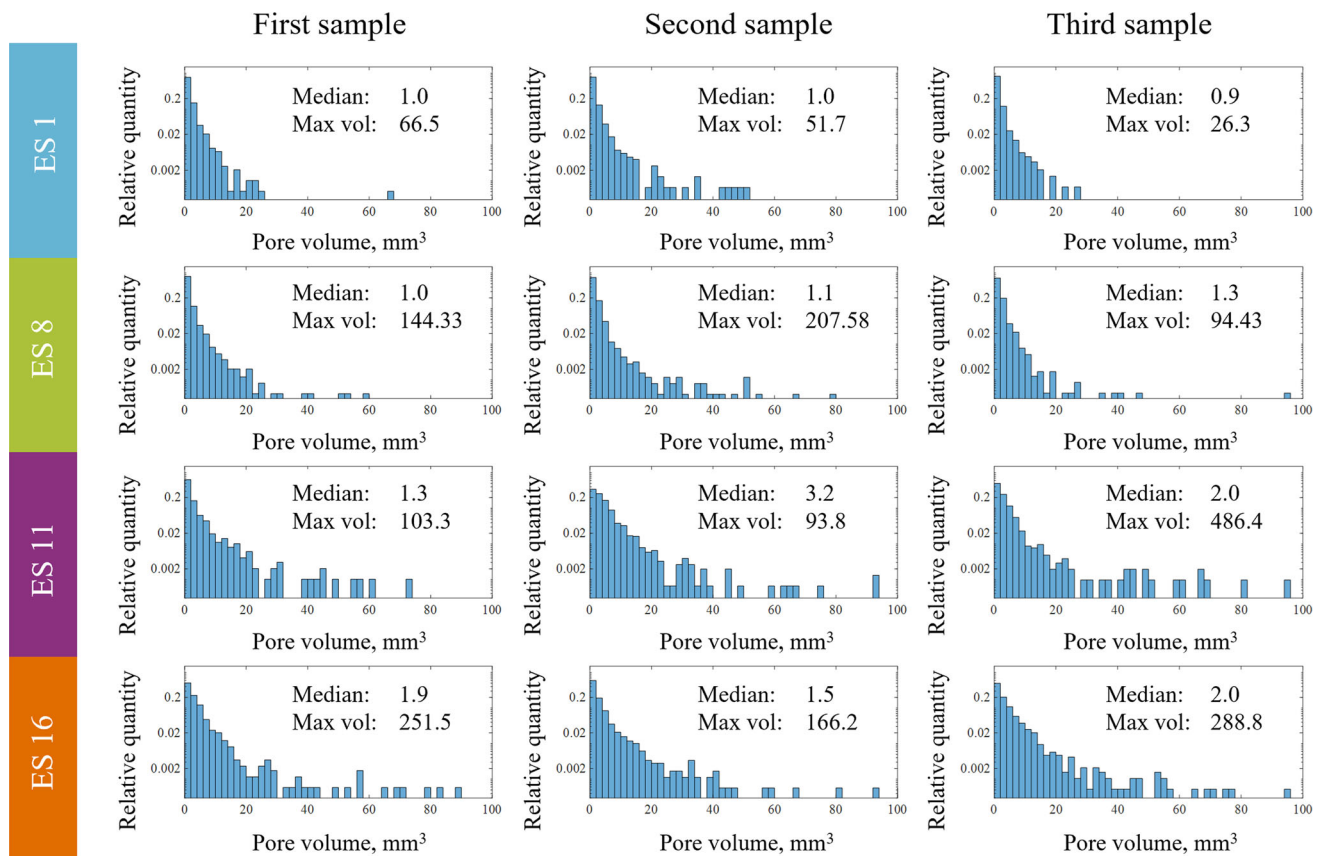


Fig. 13 X-ray microscopy cross sections with visualized wall thickness



**Fig. 14** Highlighted cells within the cross sections for the first sample of ES 1 and the second sample of ES 11



**Fig. 15** Pore volume distribution for ES 1, 8, 11 and 16

of the relative quantity is used in the histograms to represent the difference in the range of the pore volumes. Here, the relative quantity was taken into account, in order to enable a comparison over varying volumes of the investigated ROIs. The median of the pore volumes and the maximum pore size for each sample are inscribed in the histogram plots.

ES 1 shows the largest number of small pores, collected in the first bin with a bin size of two cubic millimeters. The maximum pore volume of 486 mm<sup>3</sup> is observed in the first sample from ES 11. In general, all samples of ES 11 and ES 16

feature larger cells, and therefore a higher median pore size. The mean of the median pore volumes for ES 1, 8, 11 and 16 are 1.0, 1.1, 2.2 and 1.8 mm<sup>3</sup>, respectively.

### 3.3 Correlation of Parameters Obtained from Geometrical Foam Analysis with the Mechanical Strength

Figure 16 shows that the mean plateau stress depends approximately linearly on the ratio of median cell volume to wall thickness for the four experimental series that were

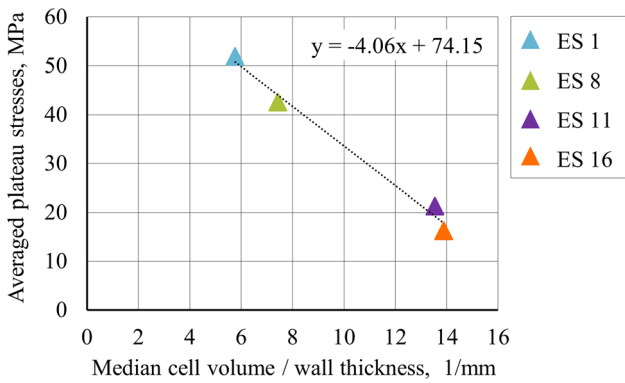


**Fig. 16** Averaged plateau stress as a function of normalized cell volume

additionally investigated with VGSTUDIO MAX. If the ratio increases, i.e. the cell volume increases and/or the wall thickness decreases, the average plateau stress decreases.

### 3.4 Virtual Foam Model

Based on the experimental observations, a virtual foam model was developed using the methods described above. The geometrical analysis involving the wall thickness and pore size distribution of the selected experimental series was used to validate this virtual model.

**3.4.1 Probability Density Function for Ball Packing.** To apply the pore size distribution to the virtual foam model, a gamma probability density function (pdf) was fitted to the pore size histogram data for each sample. To lower the complexity of the virtual foam model, a volume filter of  $V_{\text{filter}} \leq 1\text{mm}^3$  deselected the smaller pores. It was assumed, that the contribution of these small pores to the bond strength is low and that the estimated filling of these pores is incomplete due to the size of the aperture radius. The average probability density function for each experimental series is plotted in Fig. 17. The table contains the gamma coefficients for the probability density function for each sample and the mean of the experimental series.

The analysis of the pore sizes in the aluminum foam test samples (ES 1, ES 8, ES 11 and ES 16) provides valuable insights into the microstructure of the foam and the distribution of the pore size. Comparison of the parameters of ES 1 and ES 8 shows that these samples have similar characteristics in terms of pore sizes. This similarity is primarily due to the

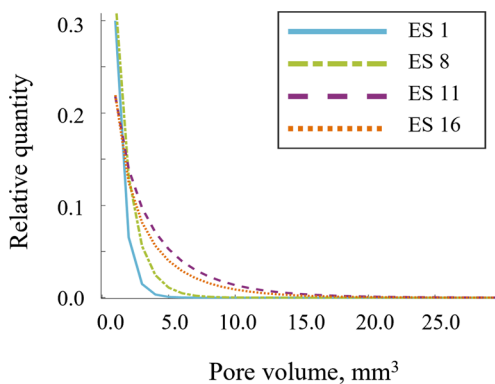


**Fig. 17** Gamma distribution and coefficients for the investigated experimental series

	ES 1	ES 8	ES 11	ES 16
First sample	0.98 / 0.21	0.85 / 0.24	0.97 / 0.35	1.19 / 0.28
Second sample	0.91 / 0.24	0.95 / 0.18	1.54 / 0.26	1.01 / 0.33
Third sample	0.97 / 0.19	1.05 / 0.18	1.24 / 0.29	1.07 / 0.35
<b>Mean ES</b>	<b>0.95 / 0.21</b>	<b>0.95 / 0.22</b>	<b>1.25 / 0.30</b>	<b>1.09 / 0.32</b>

number of smaller pores. These smaller pores may have a crucial role in influencing the mechanical properties of the foam, such as its strength and energy absorption capacity.

In contrast, the parameters of ES 11 and ES 16 show a pronounced gamma density function profile, indicating a higher number of pores in the range of  $2.5\text{-}15\text{mm}^3$ . Assuming a spherical shape of the pores, this volume range leads to aperture diameters of about one to three millimeters.

**3.4.2 Investigation of Ball Packing Parameters.** In the following, the pore volume distributions of the virtual models are compared with the estimated pore volume distributions of ES 1, 8, 11 and 16, where each experimental series consisted of three test samples. With the average coefficients for the gamma probability density function, one virtual model was created for each experimental series in order to investigate the influence of the body goal parameter of the ball packing algorithm. The relative quantity of the pore volumes is shown in the histograms of Fig. 18. The bin width of each bar has been set to two cubic millimeters in the diagrams. Here, the body goal is varied from  $bg = 0.5$  to  $bg = 0.7$  with the objective to find a suitable value.

With the body goal  $bg = 0.5$  an overfitting of large pore volumes can be observed, while a body goal of  $bg = 0.7$  leads to an overfitting in the smaller pore volume range. A poor fit can be seen in the first volume range ( $0\text{-}2\text{mm}^3$ ) for all parameter variations. In the experimental series, outliers were observed, with pore volumes reaching up to  $500\text{mm}^3$ , which were not generated by the virtual model.

With the given Voronoi dataset, created from the generation point set of the ball-packing algorithm, virtual models of the foam structures were created. The cutting plane was set in all models to  $z = 10\text{mm}$ , which is the half of the cube edge length. As seen in Fig. 19, the body goal  $bg = 0.5$  leads to larger pore volumes, which decrease with higher values of the body goal.

These observations highlight the need for careful examination and fine-tuning of the body goal parameter to ensure an accurate representation of the foam pore distribution. In addition, outliers in the pore size for experimental produced aluminum foams should be considered further. For a better fit in the first volume container, a volume filter is required. The performance of the virtual foam model with varying body goal is evaluated in the following.

**3.4.3 Evaluation of the Model Performance.** To evaluate the performance of the virtual foam model, the difference in each bin of the pore volume histogram was calculated. The

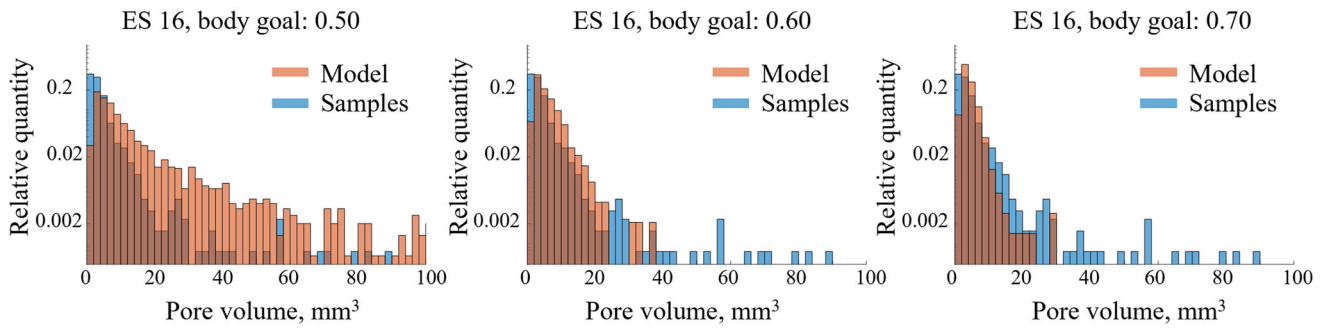


**Fig. 18** Comparison of pore size distribution of virtual foam models and experimental test samples

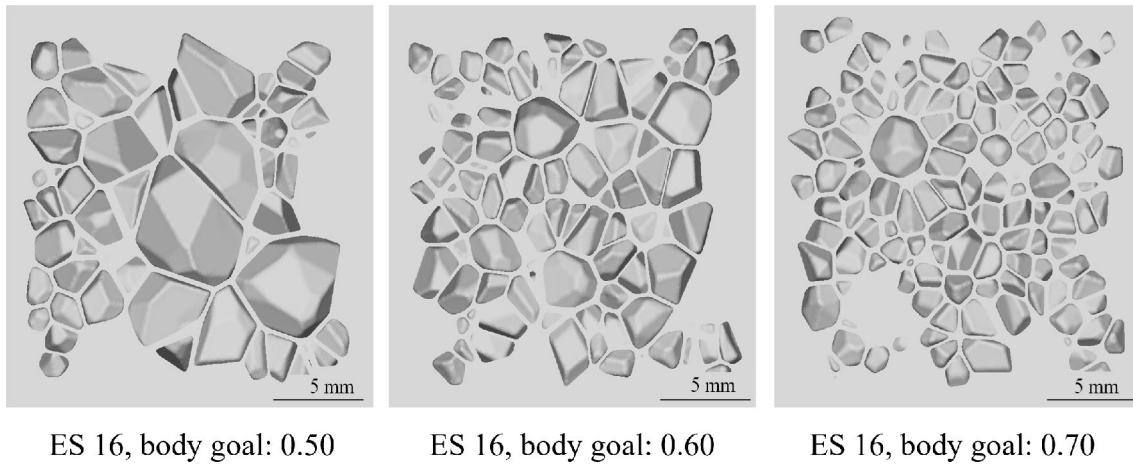


**Fig. 19** Virtual foam model with triangular surface mesh for various packing densities

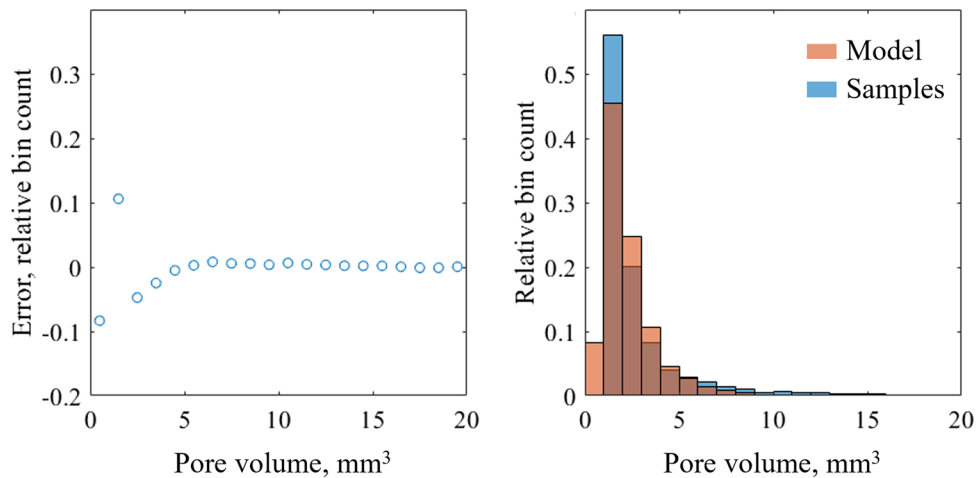


**Fig. 20** Error in relative bin counts between virtual model and experimental series for ES 1

Root Mean Square Error (RMSE) was determined with these values. The median of the pore volumes was also taken into account to compare the experimental series with the virtual foam model. In Fig. 20 the error in the relative bin counts is illustrated exemplarily for ES 1. The bin width for the error calculation is one cubic millimeter and the volume filter  $V_{\text{filter}} \leq 1\text{mm}^3$  was used to erase the smaller pores in the experimental data. The error is the highest in the first bin containers and decreases with increasing pore volume. Due to the volume filter, the first bin should be empty. However, in the

first bin of the virtual foam model a large error is present.

As the volumes of the Voronoi cells are calculated before the smoothing and remeshing step, some cells appear to be smaller than the designed minimum cell size of one cubic millimeter. This sequence in the model set-up is necessary, as the smoothing and remeshing of all Voronoi cells within the cubic RVE requires a high computational effort.

To find the suitable body target parameter for each virtual foam model representing a sample from the experimental series, the RMSE of the pore volume over all bins and the error of the

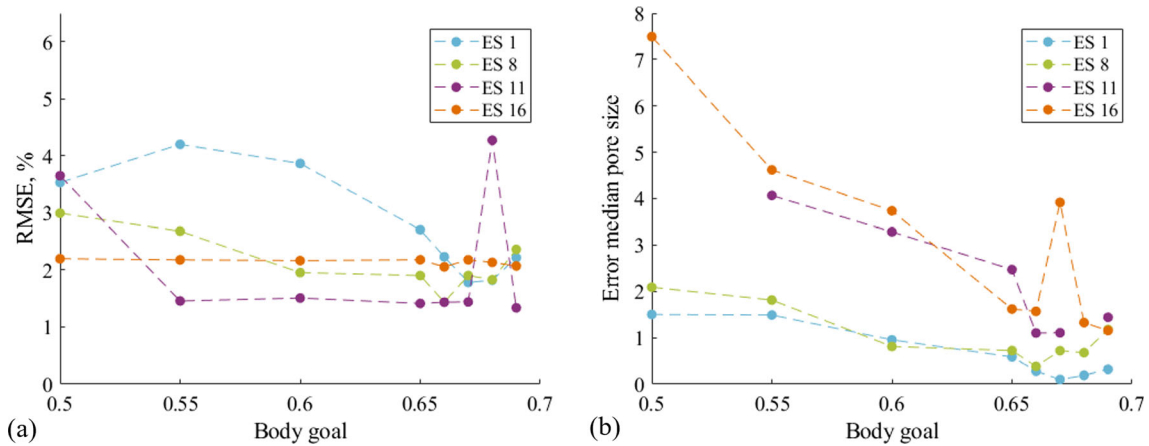


**Fig. 21** Root mean square error of the pore volume (a) and absolute error in the median pore size (b)

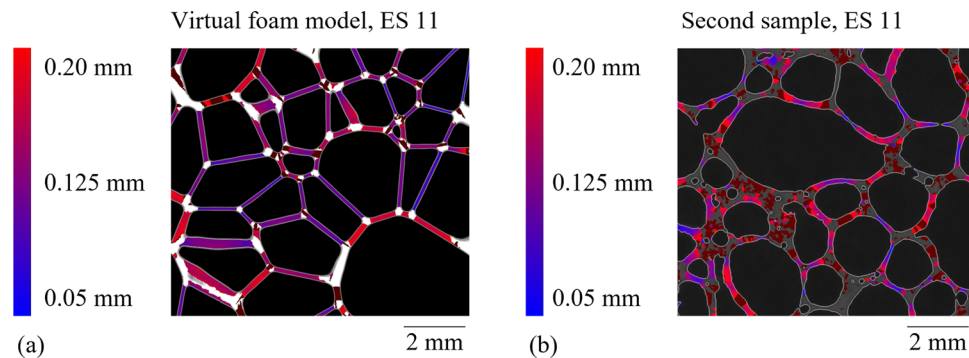


**Fig. 22** Comparison of the foam structure of the virtual foam model (a) with a sample from ES 11 (b)

median pore size were considered. The results are shown in Fig. 21, with the RMSE for each body goal parameter and for each experimental series on the left and the error in the median pore size on the right.

With increasing body goal, the error in the median pore size is decreasing for almost all experimental series. In ES 11 and ES 16 a peak with  $bg = 0.67$  and  $bg = 0.68$  is visible. The lowest median error is achieved as 0.2 for ES 1 with  $bg = 0.67$ . The RMSE ranges from 1.2 to 2.2% for all variations with a body goal higher than 0.66. The virtual foam models for ES 11 exhibits the overall lowest RMSE, with a peak at 0.68.

A qualitative comparison of the foam structure in the virtual foam model and the second sample of ES 11 is given in Fig. 22. The wall thickness is colored in the range from 0.05 to 0.2 mm. The wall thickness varies more across the length of the cell walls in the experimental sample, compared to the virtual foam model. In the sample, the wall thickness varies comparably more across the length of the cell walls than in the virtual foam model. The wall thickness for the virtual foam model was determined using the ray method as described above for the experimentally produced test samples. For this virtual foam model, a value of 0.15 mm was calculated. The mean wall thickness of the experimental series is 0.16 mm, which leads to an error of 5.6%. Since the virtual foam model represents only cells at the boundary region of the cut RVE, the statistical distribution of wall thicknesses is not as accurate. Comparing the figure and the pore size histogram, the model adequately captures the size of the pores, but it does not accurately depict their shape.

With this paper, the data basis for a later theoretical analysis of the bond strength between metal foam and additively manufactured structural components is created as a first step. For further numerical investigations, the virtual foam model can be used to determine the influence of the pore size distribution on the pore filling during the additive manufacturing process. In addition, structural-mechanical simulations of the hybrid composite are underway to determine a desired pore size distribution for the EN AW-6082 metal foams.

## 4. Conclusion

In the present study, the foaming behavior of EN AW-6082 metal foams was investigated in free foaming tests and the influences of blowing agent and foam stabilizer contents were determined. To gain insight into the process, a novel virtual foam model was developed and validated using the EN AW-6082 metal foams. The main results can be summarized as follows:

- At a furnace temperature of 750 °C and a holding time of 5 min, a porosity of 75% could be achieved in the EN AW-6082 metal foams.
- A blowing agent content of 0.5 wt.% and the use of SiC as a foam stabilizer resulted in an increase in porosity, independent of the three SiC particle sizes and volume percentages investigated.

- Heat treatment of the blowing agent TiH<sub>2</sub> did not have a significant influence on the porosity of the EN AW-6082 metal foams in the free foaming tests.
- The results of the compression tests showed a close correlation between porosity and maximum plateau stress. The highest average stress of 91 MPa was achieved at the lowest average porosity of 50.5%. At the highest porosity of 74.9%, 16 MPa were still achieved.
- The virtual foam model can predict the wall thickness with small error of  $\leq 5.6\%$ .
- The median pore size obtained from the virtual foam model decreases as the packing density of the spheres increases, with the associated numerical parameter taking values between 0.6 and 0.7 to exhibit the lowest error of all experimental series. The virtual foam model has a lower error in the median pore size when compared to experimental series with smaller pore sizes.

## Acknowledgments

Financial support by Deutsche Forschungsgemeinschaft (project ID 442092412) is gratefully acknowledged.

## Funding

Open Access funding enabled and organized by Projekt DEAL.

## Open Access

This article is licensed under a Creative Commons Attribution 4.0 International License, which permits use, sharing, adaptation, distribution and reproduction in any medium or format, as long as you give appropriate credit to the original author(s) and the source, provide a link to the Creative Commons licence, and indicate if changes were made. The images or other third party material in this article are included in the article's Creative Commons licence, unless indicated otherwise in a credit line to the material. If material is not included in the article's Creative Commons licence and your intended use is not permitted by statutory regulation or exceeds the permitted use, you will need to obtain permission directly from the copyright holder. To view a copy of this licence, visit <http://creativecommons.org/licenses/by/4.0/>.

## References

1. C. Brecher, S. Kozielski, and L. Schapp, Integrative produktionstechnik für hochlohnländer, *Wertschöpfung und Beschäftigung in Deutschland*. J. Gausemeier, H.-P. Wiendahl Ed., Springer Berlin Heidelberg, Berlin, Heidelberg, 2011, p 47–70. (in German)
2. H.-C. Möhring, M. Müller, J. Krieger, J. Multhoff, C. Plagge, J. de Wit, and S. Misch, Intelligent Lightweight Structures for Hybrid Machine Tools, *Prod. Eng. Res. Dev.*, 2020, **14**, p 583–600
3. A. Sj and A. Natarajan, Review on the Advancements and Relevance of Emerging Joining Techniques for Aluminum to Polymers/Carbon Fiber-Reinforced Polymer Lightweight Hybrid Structures, *Proc. Inst. Mech. Eng. Part L J. Mater. Des. Appl.*, 2022, **236**, p 2394–2435
4. I. Duarte, M. Oliveira, F. Garcia-Moreno, M. Mukherjee, and J. Banhart, Foaming of AA 6061 Using Multiple Pieces of Foamable Precursor, *Colloids Surf. A*, 2013, **438**, p 47–55
5. H.-M. Helwig and J. Banhart, *Helmholz-Zentrum Berlin für Materialien und Energie GmbH, Patent: Aluminiumlegierung für Metallschäume, ihre Verwendung und Verfahren zur Herstellung*, 2009, Germany (DE 10 2008 027 798 A1). (in German)
6. I. Duarte and M. Oliveir, Aluminum alloy foams: production and properties, *Powder Metallurgy*. K. Kondoh Ed., InTech, London, 2012
7. T. Miyoshi, M. Itoh, S. Akiyama, and A. Kitahara, ALPORAS Aluminum Foam: Production Process, Properties, and Applications, *Adv. Eng. Mater.*, 2000, **2**, p 179–183
8. G. Lange, *Metallschäume, Herstellung, Eigenschaften, Potenziale und Forschungsansätze—mit Schwerpunkt auf Aluminumschäume*, De Gruyter, Berlin, Boston, 2020. (in German)
9. M. de Giorgi, A. Carofalo, V. Dattoma, R. Nobile, and F. Palano, Aluminum Foams Structural modeling, *Comput. Struct.*, 2010, **88**, p 25–35
10. Y. Chen, R. Das, M. Battley, and Z. Xu, Compressive and Shear Strengths of the Ductile Closed-Cell Kelvin and Weaire-Phelan Foams Along the Lattice Direction [100], *Thin-Walled Struct.*, 2018, **132**, p 237–249
11. M. File, R. Cseke, D. Huri, G. Balogh, and T. Mankovits, Finite Element Analysis of Closed-Cell Aluminum Foam Approximated with Weaire-Phelan Unit Cell Structure, *IOP Conf. Ser. Mater. Sci. Eng.*, 2022, **1246**, p 12002
12. R. Dai, M. Wang, D. Wang, Z. Hu, M.D. Green, and Q. Nian, Understanding Mechanical Behavior of Metallic Foam with Hollow Struts using the Hollow Pentagonal Dodecahedron Model, *Scr. Mater.*, 2020, **182**, p 114–119
13. S. Wang, Y. Ma, Z. Deng, and X. Wu, Two Elastically Equivalent Compound Truss Lattice Materials with Controllable Anisotropic Mechanical Properties, *Int. J. Mech. Sci.*, 2022, **213**, 106879
14. C. Redenbach, I. Shklyar, and H. Andrá, Laguerre Tessellations for Elastic Stiffness Simulations of Closed Foams with Strongly Varying Cell Sizes, *Int. J. Eng. Sci.*, 2012, **50**, p 70–78
15. C. Redenbach, Microstructure Models for Cellular Materials, *Comput. Mater. Sci.*, 2009, **44**, p 1397–1407
16. N. Michailidis, E. Smyrniotis, G. Maliaris, F. Stergioudi, and A. Tsouknidas, Mechanical Response and FEM Modeling of Porous Al under Static and Dynamic Loads, *Adv. Eng. Mater.*, 2014, **16**, p 289–294
17. B. Matijasevic, S. Fiechter, I. Zizak, O. Görke, N. Wanderka, P. Schubert-Bischoff, and J. Banhart, Decomposition behaviour of as-received and oxidized TiH<sub>2</sub> Powder, In *Symposium Metallschäume*, 2004
18. B. Matijasevic and J. Banhart, Improvement of Aluminum Foam Technology by Tailoring of Blowing Agent, *Scr. Mater.*, 2006, **54**, p 503–508
19. B. Matijasevic-Lux, J. Banhart, S. Fiechter, O. Görke, and N. Wanderka, Modification of Titanium Hydride for Improved Aluminum Foam Manufacture, *Acta Mater.*, 2006, **54**, p 1887–1900
20. A.P. Mangan and R.T. Whitaker, Partitioning 3D Surface Meshes using Watershed Segmentation, *IEEE Trans. Vis. Comput. Gr.*, 1999, **5**, p 308–321
21. G. Voronoi, Nouvelles Applications des Paramètres Continus à la Théorie des Formes Quadratiques. Deuxième Mémoire. Recherches sur les Paralléloèdres Primitifs, *J. Reine Angew. Math. (Crelles J.)*, 1908, **1908**, p 198–287. (in French)
22. F. Aurenhammer, Voronoi Diagrams—A Survey of a Fundamental Geometric Data Structure, *ACM Comput. Surv.*, 1991, **23**, p 345–405
23. F. Timmann, A. Hürkamp, and K. Dröder, Numerical analysis of a manufacturing process for hybrid structures combining extruded aluminum profiles and additive manufacturing, In *Composite Construction Laboratory (ed), Proceedings of the 20th European Conference on Composite Materials—Composites Meet Sustainability (Vol 1-6), Volume 4—Modeling and Prediction*, EPFL Lausanne, Composite Construction Laboratory, Lausanne, 2022, pp 977–984
24. C.T. Loop, *Smooth Subdivision Surfaces Based on Triangles*, Master Thesis, University of Utah, 1987
25. D.A. Field, Laplacian Smoothing and Delaunay Triangulations, *Commun. Appl. Numer. Methods*, 1988, **4**, p 709–712
26. T.J. Black and A.F. Cheviakov, 3DRSP: Matlab-Based Random Sphere Packing Code in Three Dimensions, *SoftwareX*, 2022, **18**, 101051
27. R.E. Walpole, R.H. Myers, S.L. Myers, and K. Ye, *Probability & Statistics for Engineers & Scientists*, MyStatLab update, Ninth edition, Pearson, Boston, 2017
28. P. Weigand and J. Banhart, Untersuchungen des Schäumens von Metallen, In *Symposium Metallschäume*, 1997. (in German)

29. K. Heim, F. García-Moreno, and J. Banhart, Particle Size and Fraction Required to Stabilise Aluminum Alloy Foams Created by Gas Injection, *Scr. Mater.*, 2018, **153**, p 54–58

**Publisher's Note** Springer Nature remains neutral with regard to jurisdictional claims in published maps and institutional affiliations.